ACS ENGINEERING Au
AN OPEN ACCESS JOURNAL OF THE AMERICAN CHEMICAL SOCIETY

pubs.acs.org/engineeringau
Article

Quantifying the Impact of Intraparticle Convection within Fixed Beds Formed by Catalytic Particles with Low Macro-Porosities

Stylianos Kyrimis, Matthew E. Potter, Robert Raja, and Lindsay-Marie Armstrong*

Cite This: ACS Eng. Au 2023, 3, 335−351
Read Online

ABSTRACT: Computational fluid dynamics (CFD) modeling plays a pivotal role in optimizing fixed bed catalytic chemical reactors to enhance performance but must accurately capture the various length- and time-scales that underpin the complex particle−fluid interactions. Within catalytic particles, a range of pore sizes exist, with micro-pore scales enhancing the active surface area for increased reactivity and macro-pore scales enhancing intraparticle heat and mass transfer through intraparticle convection. Existing particle-resolved CFD models primarily approach such dual-scale particles with low intraparticle macro-porosities as purely solid. Consequently, intraparticle phenomena associated with intraparticle convection are neglected, and their impact in the full bed scale is not understood. This study presents a porous particle CFD model, whereby individual particles are defined through two distinct porosity terms, a macro-porosity term responsible for the particle's hydrodynamic profile and a micro-porosity term responsible for diffusion and reaction. By comparing the flow profiles through full beds formed by porous and solid particles, the impact of intraparticle convection on mass and heat transfer, as well as on diffusion and reaction, was investigated.

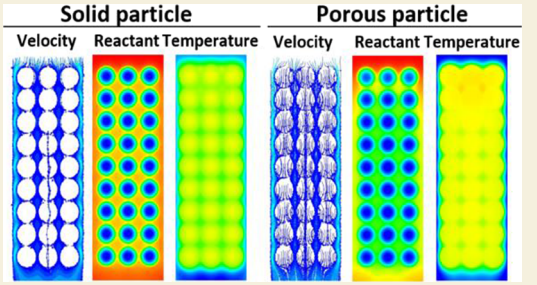

KEYWORDS: *computational fluid dynamics (CFD), porous particle, macro-porosity, micro-porosity, resolved particle CFD (PR-CFD), discrete element method (DEM), fixed bed chemical reactors, intraparticle convection*

INTRODUCTION

Heterogeneous fixed bed chemical reactors are vital for the production of key fuels and chemicals, such as methanol, ethylene, sulfuric acid, and ammonia.[1−3] Due to their low cost, ease of separation of gas (i.e., reactants and products) and solid (i.e., catalytic particles), and compact design,[4−6] they have been the predominant reactor type for heterogeneous gas-phase reactions[7] for more than 70 years.[4] Fixed bed systems involve a broad range of length scales,[8,9] spanning the nanometer molecular interactions between reagents and active sites, to the local (cm-scale) and global (up to m-scale) temperature hot spots and pressure drop, all of which need to be understood. In recent years, computational fluid dynamics (CFD) models have been instrumental in the advancement of fixed bed chemical reactors, which are utilized both as investigative and as optimization tools.[7,9−13] In particle-resolved CFD (PR-CFD) models, realistic particle arrangements are generated primarily through the discrete element method (DEM),[7,14,15] and the individual particles are resolved and meshed. Particle sizes and shapes within the packed bed can either be mono-[16−18] or poly-dispersed[19−22] in nature, with modern DEM-based beds implementing multiple particle shapes, such as spherical, cylindrical, or Raschig rings.[14,15,17,18,23−26] PR-CFD models yield key information regarding the interconnected nature of the physicochemical phenomena during operation of the fixed bed system.[17,18,23] Specifically, their ability to consider the impact of the geometrical bed structure to predict the interparticle heat and mass transfer yields highly valuable insights for reactor engineering.[27−29] Fixed bed reactors include different levels of "porosity" (Figure 1). The particles (gray spheres in Figure 1a) are immobile, having interconnected gaps between them, referred to as "interparticle network", where reagents can flow through. Interparticle porosity, ε_{Inter}, or bed void fraction, refers to the total volume of the fixed bed, V_{Bed}, minus the catalyst volume, V_{Solid}, assuming the catalytic particles to be purely solid. In most PR-CFD studies, the catalytic particles are treated as solid for the purpose of intraparticle flow, with the external particle surface being modeled as an impermeable wall.[8,17,18,23,30] By enforcing the no-slip boundary condition on their surface, viscous flow, and thus intraparticle convection, does not penetrate the intraparticle structure, where only species diffusion is assumed to exist. However, catalytic porous media with multi-scale porosities are routinely used for various applications, reinforcing the need for advanced CFD models,

Received: May 5, 2023
Revised: August 25, 2023
Accepted: August 25, 2023
Published: September 7, 2023

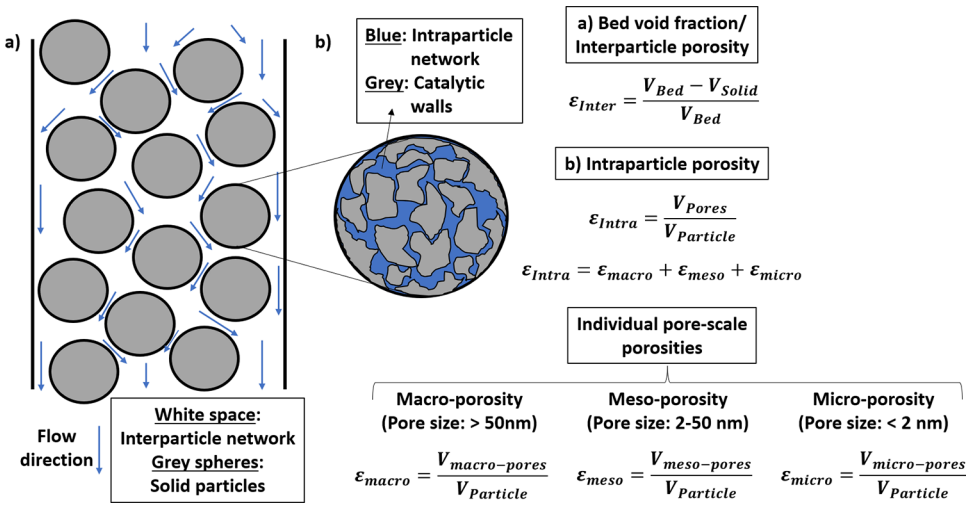

Figure 1. Simplified schematic of the (a) catalytic bed and (b) catalytic particle, along with the definition of the different porosity terms.

able to reproduce the complex intraparticle structure and its impact on all aspects of physicochemical phenomena, including intraparticle convection.[28,31−35]

Catalytic particles are often porous, formed by a compressed catalyst, allowing for reagents to enter and diffuse through them.[36,37] Based on the catalyst nature and framework, the catalyst either contains macro-pores (pore sizes >50 nm), meso-pores (pore sizes between 2 and 50 nm), or micro-pores (pore sizes <2 nm).[37,38] Catalysts can also be tailored for specific purposes, as demonstrated by the recent advancements in hierarchical catalysts.[39−41] For example, hierarchical zeolites combine micro- with meso- or macro-pores for enhanced intraparticle active site access and reagent transport.[42,43] Further, as the catalytic powder is compressed into a particle, cracks, fissures, or open structures are formed, consisting of interconnected pores, dead-end pores, or closed pores,[44] with pore diameters ranging from micrometers to Angstroms.[37,38] These pores formed within the particles are referred to as "intraparticle network", and the total pore volume they occupy, V_{Pores}, divided by the total volume of the particle, V_{Particle}, defines the particle's total intraparticle porosity, $\varepsilon_{\text{Intra}}$. This intraparticle porosity is the sum of the macro-, meso-, and micro-porosities of the particle,[33] referring to the total pore volume occupied by macro- ($V_{\text{macro - pores}}$), meso- ($V_{\text{meso - pores}}$), and micro-pores ($V_{\text{micro - pores}}$) and divided by the total particle volume. The predominant methods used to experimentally determine pore size distribution and intraparticle porosity of porous catalysts are through N_2 adsorption porosimetry, mercury porosimetry, or density functional theory.[45−47] However, these methods primarily estimate the porous nature of the catalytic powder and are not employed to assess the intraparticle porosity after the powder has been compressed into a particle.

Each of these pore-scales offers distinct advantages to the porous medium. Specifically, macro-pores allow convective flow to traverse the medium, increasing the effective heat and mass transfer compared to what would be possible solely through intraparticle diffusion.[34,35] On the contrary, there is no convection through the micro-pores, and the role of this pore-scale is to maximize the effective surface area and thus the reactivity of the porous medium.[34,35] In fact, catalytic porous media with dual-scale porosities have been introduced at different applications to reinforce heat and mass transfer through intraparticle convection.[28,31−35] These can be broken down into porous media with large macro-porosities, above 0.5, and with low macro-porosities, below 0.5. For the latter, Yang et al. examined the intraparticle flow phenomena within a porous particle containing 10 nm meso-pores and 0.1 mm macro-pores.[32] By ranging the level of macro-porosity, they identified that a critical macro-porosity exists between 0.6 and 0.7, which changes the importance of the surface friction drag and the body pressure drag within the particle.[32] A key example of dual-scale particles with large macro-porosities is open-foam particles, which exhibit macro-porosities, $\varepsilon_{\text{macro}}$, Figure 1, above 0.8, with macro-pore diameters in the order of mm.[48−52] Due to the large macro-porosities of these structures, intraparticle convection plays a prominent role in the hydrodynamic profile of the bed, reducing the pressure drop, increasing the distribution of residence times, and reducing the heat transfer rate between fluid and solid.[50,52−55] For the former, Solsvik and Jakobsen investigated the impact of dual-porosity distribution, i.e., 1 nm micro-pores, 15 nm meso-pores, and total intraparticle porosity ≤0.5, on the reactor's performance, using methanol synthesis as a test reaction.[56] Their results revealed that reactor's performance is sensitive to the dual-scale porosity distribution as it is the primary driving factor of intraparticle diffusion rate.[56] Donaubauer et al.[57] investigated the impact of the intraparticle pore structure on the diffusive transport and the effectiveness factor by studying a meso-porous particle, with a pore diameter of 15 nm and an intraparticle porosity of 0.5. Four key parameters were considered to characterize the intraparticle structure, specifically intraparticle porosity, tortuosity, pore diameter, and thermal conductivity.[57] Intraparticle porosity was the most influential parameter on the effectiveness factor, followed by tortuosity, pore diameter, and finally thermal conductivity.[57] Dong et al.[33] investigated the impact of the intraparticle structure, in terms of micro- and macro-porosity and of micro- and macro-pore diameters, on n-butane oxidation. The catalytic particles considered contained micro-pores of 1 nm and macro-pores of 100 nm and had an overall intraparticle porosity of 0.5. They observed that catalysts with dual-scale porosities outperformed catalysts with only a single porosity scale, with macro-porosity and micro-pore diameter being the predominant structural parameters affecting performance.[33] For macro-porosities below 0.1, diffusion is rate-limiting,

https://doi.org/10.1021/acsengineeringau.3c00015
ACS Eng. Au 2023, 3, 335−351

restricting reactant access to the interior surface; as macro-porosity increased, the inner particle surface area became more easily accessible and performance increased.[33] However, for macro-porosities above 0.3, catalyst performance was reduced due to the reduction of the available surface area.[33]

The superior performance of multi-pore-scale catalytic particles with low macro-porosities (≤0.5), compared to single-pore-scale particles,[33,56] makes these particles highly valuable for the chemical industry. However, the transport phenomena, and specifically the level of macro-porosity below which convection starts becoming negligible, are not clearly understood. Most literature studies investigating low macro-porosity particles[57−60] reported that intraparticle convection was negligible in the single-particle scale, with diffusion being the predominant transport mechanism. The rate of intra-particle diffusion was determined as a key transport phenomenon in the study of Partopour and Dixon.[23] They investigated the behavior of a fixed bed reactor system used for ethylene oxidation under dynamic operating, specifically during the shut-off (100 s duration) and start-up (90 s duration) procedures.[23] Here, the catalytic particles were approached as completely solid and impermeable to convection. During start-up, convection transferred vast amounts of O_2 species within the bed. However, intraparticle diffusion limitations determined the overall reaction rate as its rate was much slower compared to that of convection.[23] In addition, during shut-off, because of the slow rate of intraparticle diffusion, O_2 remained within the particles long after the supply of feed was terminated, which could initiate chemical reactions.[23] This study showcases the behavior introduced by de-coupling convection and diffusion in the intraparticle space as the potential existence of intraparticle viscous flow would considerably alter the residence time of O_2 within the particles. On the contrary, both Kree et al.[44] and Donaubauer et al.[57,61] support that to adequately describe diffusion and momentum transport within porous particles, a combination of molecular diffusion, Knudsen diffusion, surface diffusion, and viscous flow is needed. Convective flux is the result of intraparticle pressure gradients due to temperature or concentration gradients caused by chemical reactions. In fact, Chen et al.[62] reported that intraparticle flow parameters, such as temperature, species, and pressure gradients, are dynamic and their impact changes based on the operating temperature, the particle size, and the pore diameters. Consequently, this could lead to conditions that enable intraparticle convection and enhance its magnitude. The potential existence of intraparticle convection on such particles could play a pivotal role in all aspects of flow dynamics within the catalytic particles. This becomes evident when simplified 1D or 2D models are compared with PR-CFD models. Specifically, by not reinforcing the de-coupling between intraparticle convection and diffusion in the intraparticle space, the simplified models predict faster reaction rates compared to PR-CFD models.[17,18,63] This is because, when combined, diffusion and convection increase the local concentration of reactants and thus the reaction rate. Dixon et al.[64,65] performed a study where intraparticle diffusion and chemical reactions within a solid particle were compared with those within a porous particle. They observed that, for the porous pellet, velocity, and thus convection, penetrated a small distance into the intraparticle space.[64] Furthermore, the porous particle exhibited higher temperatures compared to the solid particle, a result that was attributed to intraparticle convection transferring enthalpy within it.[64] However, the impact of intraparticle convection in the full catalytic bed is yet unclear.

Conclusively, theoretical investigations of catalytic particles based on PR-CFD models all treat catalytic particles as completely solid. This approach prevents the application of PR-CFD models to more complex particle morphologies, such as hierarchical catalysts or particles with dual-scale porosities. There is thus a critical need for the development of CFD models capable of capturing the multi-scale pore structure of catalytic particles. Such CFD models can lead to a deeper understanding of how the intraparticle structure affects all aspects of flow and physicochemical phenomena, both in the individual particle-scale and the full bed-scale. We focus here purely on catalytic particles with low macro-porosities, i.e., below 0.5, as they exist in-between the spectrum of a completely solid particle and an open-cell foam-type particle. In our previous work, we have investigated the performance of SAPO-34 for EtOH dehydration.[19,66,67] The strong acid sites and small micropores of SAPO-34 made it highly selective for ethylene formation.[66,67] For this system, we have previously demonstrated the potential of CFD models, developed for ANSYS Fluent, as investigate tools.[66,67] Moreover, by mapping the internal structure of the bed, we identified its highly heterogeneous nature, consisting of particles with a wide range of sizes, shapes, and orientations,[19] leading to flow profiles with large velocity and pressure gradients.[22] However, the internal structure of the SAPO-34 particles was not discussed. Here, through experimental characterization, the porous nature of the SAPO-34 particles is evaluated. To understand how intraparticle convection can affect the reactor's performance, beds formed by porous particles (PPs) are developed for ANSYS Fluent, and their behavior is compared with analogous PR-CFD solid particle beds. The intraparticle structure of the individual porous particles is defined by two macro- and micro-porosity terms, with the former affecting its hydrodynamic profile, and thus intraparticle convection, and the latter affecting reaction and diffusion rates. By not treating the particle as purely solid, the PP model can quantify the impact of intraparticle convection in all aspects of flow dynamics on the full bed scale.

METHODOLOGY

This study utilizes the experimental setup and reaction framework from our previous work[19,66] on ethanol dehydration from SAPO-34, with the catalyst synthesis and characterization, reactor setup, and reaction kinetics being presented in Section 1 of the electronic Supporting Information. The setup and methodology of the PR-CFD and of the PP models are described here. For all simulations herein, ANSYS Fluent, version 2019 R2 is used. A description of the conservation of mass and momentum equations that underpin both models is given in Section 2 of the electronic Supporting Information.

Particle-Resolved CFD (PR-CFD) Model

Three particle geometries are considered, consisting of 1, 27, and 81 particles, as presented in Figures A8, A10, and A12, of the electronic Supporting Information, respectively. The particle(s) are surrounded by a fluid mixture and are enclosed within a cylindrical (particle case) or an orthogonal (bed cases) box, with the box geometry being used to reduce the empty space around the particles and thus the size of the computational mesh. Each particle was modeled as a perfect sphere with a diameter of d_p = 400 μm. In the bed cases, the

https://doi.org/10.1021/acsengineeringau.3c00015
ACS Eng. Au 2023, 3, 335−351

particles were separated from each other by a distance of 6.25% d_p to avoid complications due to contact point treatment. The PR-CFD geometries are meshed with a tetrahedral mesh, with elements of $2e^{-5}$ m in size. Around the surface of the particle(s) and in both the solid and the fluid region, a 2-layered inflation zone was considered with a thickness of 1.25% $d_p/2$, resulting in an inflated mesh of 2.5% $d_p/2$ total thickness. The final meshes consisted of 1.1, 9.8, and 27.5 M elements in the 1-, 27-, and 81-particle cases, respectively, with an average orthogonal quality of ≈0.79 for all three. The final meshes for the single particle and 27-particle bed can be seen in Figures A6a and A8a of the electronic Supporting Information, respectively.

The conservation of energy equation is presented here to help distinguish between the methodologies of the PR-CFD and the PP model. Two phases exist in the PR-CFD model, the solid phase, i.e., the particles, and the fluid phase, i.e., the species mixture. Each phase is solved using a steady-state conservation equation, as per eqs 1 and 2, respectively.[68]

Fluid part

$$\nabla \cdot \left(\vec{v}_f \left(\rho_f \frac{h}{M_{w,f}} + \rho_f \frac{v_f^2}{2} \right) \right) = \nabla \cdot \left(k_f \nabla T_f - \sum_i \frac{h_i}{M_{w,i}} \vec{J}_i + (\bar{\bar{\tau}}_f \cdot \vec{v}_f) \right) + S_h$$

Convection | Conduction | Diffusion | Dissipation | Reaction

Solid part

$$\nabla \cdot (k_s \nabla T_s) + S_h = 0$$

Conduction | Reaction

Subscripts "f" and "s" denote the fluid mixture (calculated based on mass-weighted mixing law) and the solid phase, respectively. The solid particle has a density, ρ_s, equal to the material density of SAPO-34, i.e., 1480 kg/m^3 as per,[69] the specific heat capacity, $C_{p,s}$, of aluminum, i.e., 871 J/(kg·K), and a pellet thermal conductivity, k_s, of 1 W/(m·K).[18,23,70]

Viscous dissipation is generally considered negligible[68] and the fundamental PR-CFD model in ANSYS Fluent treats solid regions as impermeable to fluid, i.e., no slip velocity on the solid surface, thus intraparticle velocity, pressure, and species are omitted. Given the majority of active sites are located within the intraparticle space,[37] it is expected that reaction is predominant there rather than on the particle surface. To bypass this and capture intraparticle diffusion effects, the method of Dixon et al.[64] is implemented, whereby scalar conservation equations are introduced, eq 3, which can exist in both the solid and the fluid regions.[68]

$$\nabla \cdot (\rho_f \vec{v}_f \varphi_i - \rho_f \mathcal{D}_{eff,i} \nabla \varphi_i) = R_{i,j}$$

Convection | Diffusion | Reaction

Equation 3 replaces the species conservation equations, as these arbitrary scalars, φ_i, are equivalent to the species mass fractions, Y_i. Thus, any changes to the species, e.g., due to chemical reactions, are instead applied on these scalars. Then, at the end of each iteration, the mass fraction of each of the involved species takes the value of its respective scalar quantity, i.e., $Y_i = \varphi_i$. Any properties necessary to calculate flow parameters, e.g., molecular weight, are considered equal to those of the respective species that each scalar represents. The standard species conservation equation in Fluent offers limited options to modify diffusion transfer, so implementing the scalar conservation equation, eq. 3, provides a method to implement more complex diffusion mechanisms, such as the DG model.[18,71]

Scalar conservation is dependent on convective transfer, diffusive transfer, and destruction and/or production due to chemical reactions. In the fluid region, no chemical reactions occur, as only heterogeneous reactions take place, while diffusion transfer, dictated by the local diffusion coefficient, $D_{eff,i}$, is based on bulk diffusion mechanisms. Within the solid region, reactions are dictated by Arrhenius equations, intraparticle velocity is zero, i.e., no convective transfer, and intraparticle diffusion is defined by the DG model, described in Section 2.1 of the electronic Supporting Information. These distinctions are visually described in Figure A10a. Diffusion is determined using a micro-porosity term, which, for the SAPO-34 particles, is determined equal to 0.45, as discussed later.

The reaction mechanism is a two-step dehydration of ethanol (EtOH), C_2H_5OH, to ethylene, C_2H_4, through the formation of a diethyl ether (DEE), $(C_2H_5)_2O$, intermediate, i.e., eq 4 followed by eq 5, as formulated in our previous work.[66] The rate of reaction in the intraparticle space takes the form of two 2nd-order Arrhenius equations, eq 6. The pre-exponential factor, A_j, and activation energy, E_j, for each reaction are presented in Table A2 in the electronic Supporting Information. The subscripts "i" and "j" refer to the scalar species and the reaction pathway, respectively.

$$R_1: 2 \cdot C_2H_5OH \rightarrow (C_2H_5)_2O + H_2O, \Delta H = -23.94 \text{ kJ/mol} \quad (4)$$

$$R_2: (C_2H_5)_2O \rightarrow C_2H_5OH + C_2H_4, \Delta H = +69.86 \text{ kJ/mol} \quad (5)$$

$$R_{i,j} = \rho_s \sum_{j=1}^{2} \eta_{i,j} M_{w,i} \cdot A_j \cdot \exp\left(\frac{-E_j}{R T_s} \right) \cdot \left(\frac{\rho_f \varphi_i}{M_{w,i}} \right)^2 \quad (6)$$

All conservation equations are treated in their steady-state form, replicating our experimental setup where the behavior of our chemical reactor is examined after a steady-state has been reached. This was validated through a time-on-stream study, where it was observed that past 30 min species concentrations remained constant. Examining the reactor under transient state would result in considerably different transport phenomena. In fact, Partopour and Dixon observed that, under transient conditions, intraparticle reactant gradients were present due to the different rates of convection and diffusion.[23] Such concentration gradients could extent the reaction rate even after the reactor operation has been terminated.[23] While these conclusions are key, studying the reactor under transient conditions will further complicate model development which is the scope of this study. Hence, at this stage, steady-state was considered, but the model can be utilized in a follow-up study to explore the transient state scenario.

PP Model

As its basis, the PP model utilizes the PM approach whereby the particle(s) are not resolved and only the fluid phase exists. In the standard PM approach, the impact of the solid phase is considered through two modifications in the conservation equations. Specifically, the fluid's velocity, $\vec{v}_f$, is approached through the superficial velocity, $\vec{v}_{PM} = \varepsilon_{macro} \vec{v}_f$, where ε_{macro} is the macro-porosity of the particle.[72] The macro-porosity term determines the resistance, and thus the pressure drop, experienced by the flow due to the existence of the particle in its path. It is distinct from the micro-porosity of the

https://doi.org/10.1021/acsengineeringau.3c00015
ACS Eng. Au 2023, 3, 335−351

particles, which drives intraparticle diffusion and reaction of species. As a result, the former is only used to determine the impact of the bed structure on the pressure drop, which is approximated by a momentum sink, eq 7, determined by the Ergun equation.[73] Consequently, catalytic particles in the PP model are approached through two independent porosity terms, each responsible for different physicochemical phenomena. Each of these porosity parameters can be tuned and modified independently to replicate the intraparticle porous structure. As an example, the macro-porosity term can be tuned based on the macro-pore distribution and overall macro-porosity of an actual catalytic particle, thus changing the hydrodynamic behavior accordingly. Such tuning capabilities are not possible with the PR-CFD model, which offers a strict solid description of the particles.

$$S_i = -\nabla\cdot\left(\frac{\mu_f}{\alpha}\vec{v}_{PM} + C_{Inert}\frac{1}{2}\rho_f\vec{v}_{PM}|v_{PM}|\right) \quad (7)$$

$$\frac{1}{\alpha} = \frac{150(1-\varepsilon_{macro})^2}{{d_p}^2{\varepsilon_{macro}}^3} \quad (8)$$

$$C_{Inert} = \frac{3.5(1-\varepsilon_{macro})}{d_p{\varepsilon_{macro}}^3} \quad (9)$$

In a similar method to Das et al.,[53] by knowing the spatial coordinates of the individual DEM-produced particles, as well as the volume they occupy, respective localized porous intraparticle regions can be defined through external user-defined codes. Consequently, should the computational cell fall within these intraparticle regions, a macro-porosity and viscous and inertial resistances are assigned. Otherwise, outside the intraparticle region, ε_{macro} takes a value of 1.0 (non-porous) and the viscous and inertial resistances are not applied—thus the region is considered as fluid. This distinction between inter- and intraparticle regions modifies the energy conservation equation, which is now approached by eqs 10 and 11, respectively.

Interparticle region

$$\nabla\cdot\left(\vec{v}_f\left(\rho_f\frac{h}{M_{w,f}} + \rho_f\frac{{u_f}^2}{2}\right)\right) = \nabla\cdot\left(k_f\nabla T_f - \sum_j\frac{h_j}{M_{w,j}}\vec{J}_j\right)$$

Convection | Conduction | Diffusion

Intraparticle region

$$\nabla\cdot\left(\vec{v}_{PM}\left(\rho_f\frac{h}{M_{w,f}} + \rho_f\frac{{v_{PM}}^2}{2}\right)\right) = \nabla\cdot\left(k_s\nabla T_f - \sum_j\frac{h_j}{M_{w,j}}\vec{J}_j\right) + S_h$$

Convection | Conduction | Diffusion | Reaction

Similar to the PR-CFD model, reactions will be deactivated in the interparticle space and follow eq 6 in the intraparticle space. The scalar equation theory, eq 3, is also used with the PP approach to introduce the DG diffusion model in the intraparticle region and the bulk diffusion model in the interparticle region. Finally, in a similar method to ε_{macro}, thermal conductivity will now be defined either as k_f or as k_s in the interparticle and intraparticle regions, respectively. Consequently, the PP approach solves for a single fluid phase within the bed, with different mechanisms and phenomena in the interparticle and intraparticle regions, thus approximating the effects described by the PR-CFD model. An overall schematic of the distinctions between the PR-CFD and the PP models is presented in Figure A10.

Here, despite introducing flow resistances within the PP, intraparticle convection is not constrained. As such, with the PP replicating the inter- and intraparticle phenomena of the PR-CFD model, any differences between the two can be attributed to the impact of intraparticle convection. To accurately resolve the boundary layer surrounding the catalytic particle, local mesh refinement around the particle interface is performed. This creates an inflation zone surrounding the particle interface and spanning in both the inter- and intraparticle regions, with a thickness of 2.5% $d_p/2$, making it equivalent to the inflation of the PR-CFD particle. This local refinement is visible on Figures A9b and A11b of the electronic Supporting Information for the 1- and 27-particle cases, respectively. The mesh independency study presented in Sections 4.1.1 and 4.1.2 of the electronic Supporting Information showcases the importance of this refinement layer. Specifically, it was identified that the addition of a mesh refinement layer is key to accurately capture and resolve the boundary layer formed near the particle surface. To ensure that the chosen methodology was sufficient to accurately resolve the boundary layer, Section 4.1.2 of the electronic Supporting Information compares three cases with a total of 2, 4, and 10 inflation layers by examining the flow parameters and their gradients. It was identified that increasing the number of inflation layers had a very small impact on the accuracy of the predictions, with additional layers producing sharper gradient peaks. However, the 2-layer inflation used in this study could reasonably reproduce the behavior of the 4- and 10-layer inflation cases, with considerably reduced computational resources. As a result, it was selected moving forward.

By its nature, SAPO-34 powder is a microporous catalyst with a significant pore surface area and pore volume. These were determined in-house through N_2-physisorption measurement and are presented in Section 1 of the electronic Supporting Information. Through them, the micro-porosity of the SAPO-34 powder was determined to be around 0.43−0.45 (assumed equal to 0.45), while its surface area around 510−523 m^2/g. In terms of reactivity, this large micro-porosity will significantly modify diffusion and reaction rates. However, with N_2 physisorption measurements, it is difficult to ascertain the pore size distribution and specific pore volume when the SAPO-34 powder is compressed into catalytic particles and thus the macro-porosity. SAPO-34 produces a type IV N_2-physisorption isotherm, which is characteristic of mesoporous catalysts,[74] i.e., pore sizes between 2 and 50 nm, despite being micro-porous in nature. This is due to small networks forming as the powder is dried and put under vacuum. The existence of such networks within the particles, formed during powder compression, is also expected. Unlike open-cell foam particles, however, the SAPO-34 particles do not exhibit visually distinct macro-pores, as is evident by examining the SEM picture of Figure A3 of the electronic Supporting Information. The particles are not solid either, thus intraparticle convection cannot be entirely neglected. Determining the macro-porosity with the available data is not possible as that would require mercury or helium porosimetry. Due to a lack of a systemic experimental method to accurately determine the pore size range and distribution within catalytic particles, the impact of intraparticle macro-porosity is not clearly understood.

https://doi.org/10.1021/acsengineeringau.3c00015
ACS Eng. Au 2023, 3, 335−351

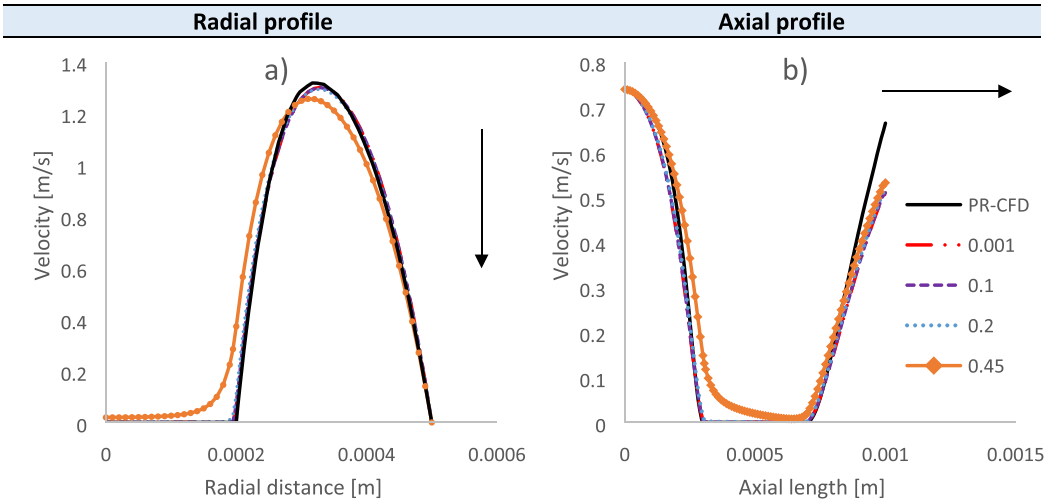

Figure 2. (a) Radial and (b) axial velocity magnitude profiles as a result of different particle macro-porosities. The results of a purely solid particle (PR-CFD) are also examined. The arrow signifies the flow direction.

However, the developed PP model can be utilized to theoretically investigate the role of macro-porosity in the heat and mass transfer, as well as in chemical performance, of individual catalytic particles. For this purpose, five different macro-porosity levels are examined, ranging from 0, i.e., solid, to 0.45, i.e., equal to the micro-porosity of SAPO-34.

Solution Setup

A mass-flow inlet was defined at the top of the geometry, with the flow rate determined experimentally through the equivalent weight hourly space velocity (WHSV). WHSV refers to the change in the feed composition and flow rate according to the mass of the catalyst within the bed. In the actual experimental runs, 0.3 g of catalyst was used. This study considers 1, 27, and 81 particle(s) are considered, which are all a negligible percentage of the entire bed volume. Thus, the equivalent WHSV values are calculated based on the entire catalyst bed. As per previous work,[19,66] the conditions considered are a WHSV of 2_{eq} h^{-1}, a mass fraction of ethanol in the inlet of around 21%, perfectly mixed with N_2, 77%, and heptane (internal standard), 2%, and a temperature of 200 °C. The considered WHSV corresponds to a particle Reynolds number of 10.3. Following the experimental reactor setup, schematically shown in Figure A4, the base of the geometry was specified as the pressure-outlet, with a gauge pressure of 0 Pa. The outer walls of the geometry were modeled as no-slip walls, with a constant temperature of 200 °C. In the PR-CFD particle-fluid interface, coupled boundary conditions for temperature and scalars were considered, allowing the exchange of heat and scalars between the two regions. This is the default interaction in the PP models as all computational cells are considered "interior" cells. In all cases, the SIMPLE scheme for pressure−velocity coupling was applied using the second-order upwind discretization for all parameters. All cases are simulated under steady-state, laminar conditions. Under-relaxation factors of 0.5 and 0.7 were used for the pressure and for the momentum/scalars, respectively. Residual targets were 3×10^{-4} for all parameters except for energy which was set to 1×10^{-6}. All cases were simulated until convergence was reached, unless specified otherwise. All simulations were performed on the IRIDIS 5 high-performance computing facility, utilizing 1 Intel Xeon 6130 2.1 GHz CPU with 139 Gb of RAM.

RESULTS

Four flow parameters, i.e., velocity magnitude, pressure, EtOH mass fraction, and temperature, are compared for each model along the axial and radial positions, as those are defined in Figure A11 of the electronic Supporting Information. The electronic Supporting Information provides accompanying 2D contour plots for each parameter and each model.

Intraparticle Macro-Porosity

The impact of changing the macro-porosity of the porous particle(s) is investigated with the 1-particle case. Four different macro-porosities are investigated, ranging from 0.001 to 0.45, with the latter being equal to the micro-porosity of the SAPO-34 particles. The value of the macro-porosity directly determines the flow resistances within the intraparticle space through eqs 7−9. In addition, a purely solid particle (PR-CFD) is also examined. The radial and axial velocity profiles are presented in Figure 2. The remaining flow parameters are presented in Figure A17.

Changing the macro-porosity of the porous particle significantly modifies all flow parameters. The smallest porosity considered, equal to 0.001, causes a massive increase in the intraparticle static pressure, reaching a peak of almost 30 Pa near the particle center (Figure A17a). This is due to the massive increase of 6 orders of magnitude in the viscous and inertial resistances when intraparticle macro-porosity is reduced from 0.1 to 0.001. A pressure change of that magnitude for the 1-particle case is not realistic. With a macro-porosity of this scale, the Ergun equations might not be suitable to describe the resistances experienced by the flow from each individual particle. Moreover, its predicted temperature is the highest among the considered macro-porosities. However, its velocity and EtOH mass fraction predictions are the closest to those of the PR-CFD model. On the contrary, the highest macro-porosity considered, equal to 0.45, predicts velocity and EtOH mass fraction profiles that deviate significantly from those of the PR-CFD model, even though its temperature predictions are the closest to it. The two intermediate porosities, equal to 0.1 and 0.2, give almost identical results across all four parameters. Some differences between the two can be observed in the interface region, at a radial distance of 0.2 mm, where the "0.1" porosity gives

https://doi.org/10.1021/acsengineeringau.3c00015
ACS Eng. Au 2023, 3, 335−351

sharper gradients in the pressure and velocity profiles that are closer to the profiles predicted by the PR-CFD model.

To better understand and interpret these results, the intraparticle velocity, resulting from different macro-porosities, is presented in Figure 3a. The macro-porosities of 0.001 and

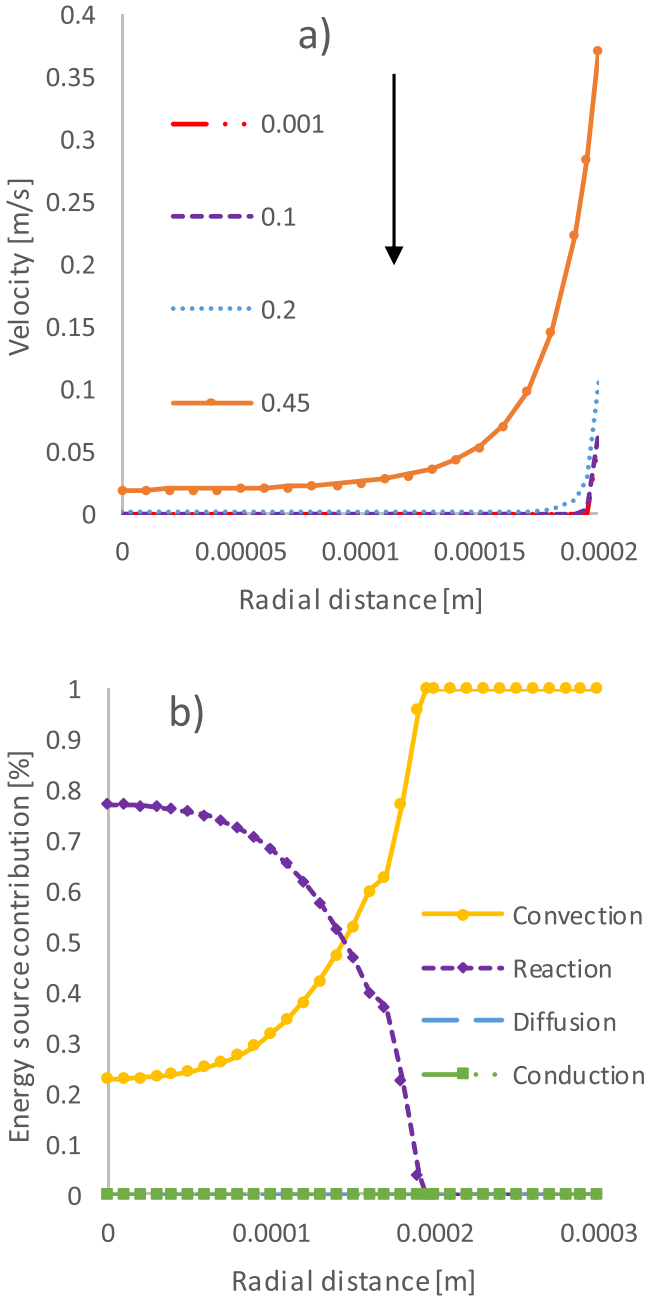

Figure 3. (a) Intraparticle velocity magnitude, predicted by the PP model utilizing different macro-porosity magnitudes, and (b) normalized contribution of energy sources for the macro-porosity of 0.1.

0.1 both result in a very similar intraparticle velocity magnitude and profile; deep in the intraparticle space, their velocity magnitude is very small, $\lesssim 3 \times 10^{-3}$ m/s on average. Near the interface and right before the free-flow region, i.e., at a radial depth of 0.195 mm, their velocity magnitude gradually increases. Macro-porosities above 0.1 start deviating from this profile, with the 0.45 porosity having a much larger average intraparticle velocity magnitude of around 0.08 m/s. This is a key observation; intraparticle velocity signifies the existence of intraparticle convective transfer, which locally changes both the species concentrations and the temperature, especially when compared to the PR-CFD model where the intraparticle velocity is zero by default. Due to the higher magnitude of flow resistances achieved by lower macro-porosities, intraparticle velocity, and thus intraparticle convection is greatly reduced. As macro-porosity increases beyond the value of 0.1, intraparticle convection becomes more influential. This is further substantiated by investigating the normalized contribution of the four energy terms, which is presented in Figure 3b for the macro-porosity of 0.1 and in Figure A18 for the remaining macro-porosities.

For the macro-porosity of 0.001, convection's contribution within the intraparticle region is very small, around 0.1% on average, and increases to a value of almost 99% solely near the interface, at a radial length above 0.195 mm. This is an almost identical behavior to that predicted by the PR-CFD model (Figure A18d), and thus, this level of macro-porosity essentially represents a solid particle. On the contrary, larger macro-porosities all result in an increasing intraparticle convection contribution, with the macro-porosity of 0.45 predicting contributions above 98% even at the center of the particle. In all cases, the impact of conduction and diffusion is very low, <1%. Conduction is one of the key heat transfer mechanisms within packed beds.[75] However, the mild exothermicity of DEE formation results in negligible temperature differences within the particle, with magnitudes around 0.1−0.2 K as per Figure A17c, and thus negligible temperature gradients. This was also observed in our previous work.[66] Consequently, intraparticle temperature in both the PR-CFD and in the PP model is practically isothermal, thus there is no driving force for conductive heat transfer. In addition, as determined by the diffusion energy term in eq 1, the magnitude of diffusive energy transfer depends on the intraparticle diffusion coefficients, $D_{\mathrm{eff},i}$, and on the exothermicity of the studied reaction. In the intraparticle space, the diffusion coefficients of species have a magnitude around 1×10^{-6}−1×10^{-5} m^2/s. Their small magnitude, combined with the mild exothermicity of the considered reaction, causes the diffusion energy term to also be negligible. As a result, the two primary energy sources here are convection and reaction. The existence of intraparticle convection changes all transfer phenomena, and thus all main flow parameters, an effect similar to what was observed for open-cell foam particles.[50,52−55] Moreover, the energy balance seen in Figure 3b verifies the observation of Dixon et al.,[64] where intraparticle convection has a significant energetic contribution in porous particles.

The results in this section clearly indicate that the morphology of the intraparticle structure affects all aspects of heat and mass transfer, as well as the chemical performance of the catalytic particles. Specifically, for macro-porosities below 0.1, the flow resistances introduced significantly reduce the magnitude of intraparticle convection. As a result, the behavior of a porous particle approaches that of a completely solid particle, and diffusion becomes the predominant intraparticle transport mechanism. On the contrary, for the macro-porosity of 0.45, the porous particle is highly permeable, thus both convection and diffusion affect the species transport. As a result, the intraparticle residence time of species is reduced, forcing the chemical performance of the particle to significantly

https://doi.org/10.1021/acsengineeringau.3c00015
ACS Eng. Au 2023, 3, 335−351

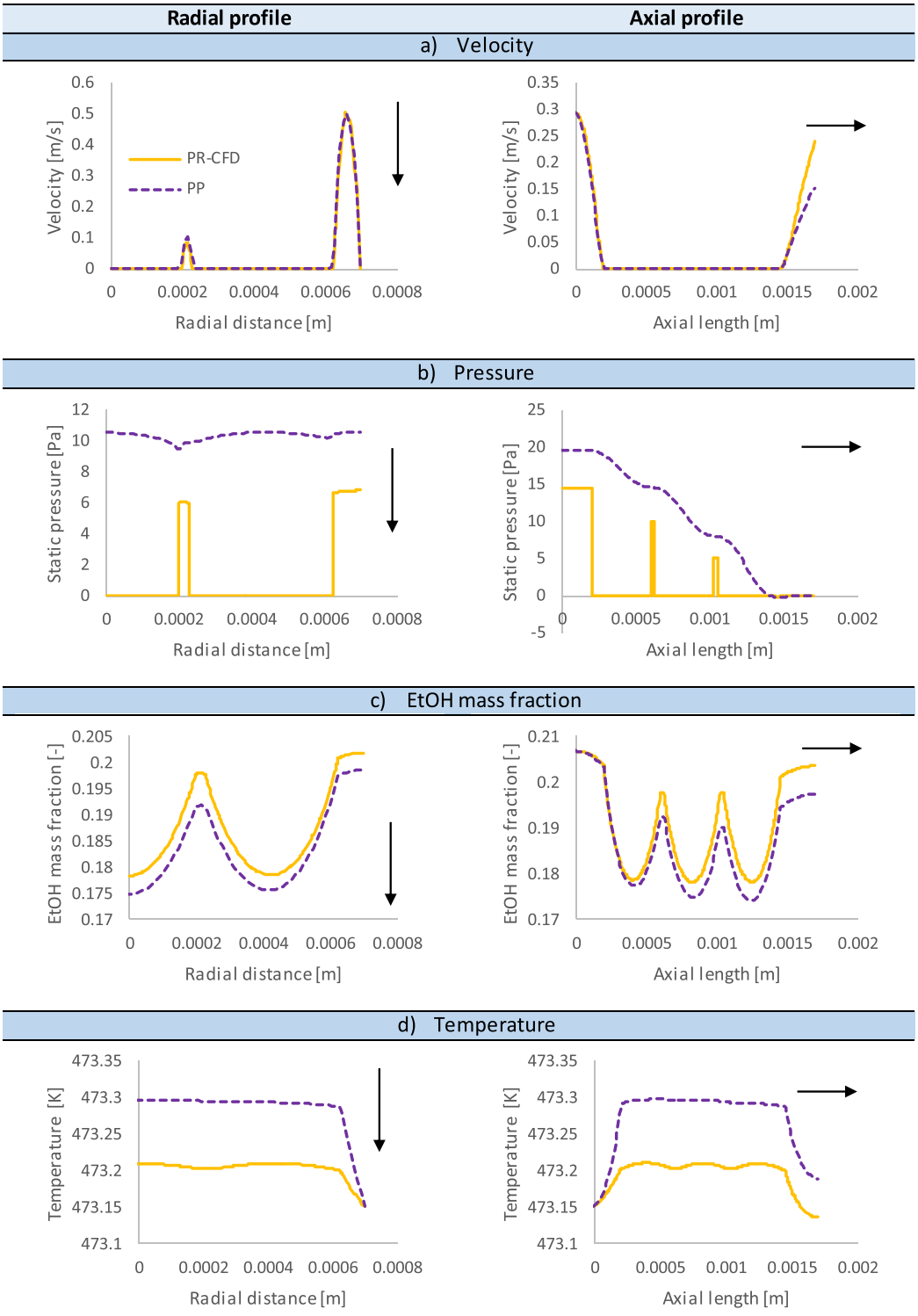

Figure 4. (a) Velocity, (b) pressure, (c) EtOH mass fraction, and (d) temperature for the 27-particle case, as predicted by the PP and the PR-CFD models. All figures share the same legend. The arrows represent the flow direction.

drop. These are key behaviors that not only affect the local but also the global bed scale. Consequently, these results can be validated in a follow-up study, with available experimental data on ethanol dehydration gathered from our laboratory-scale fixed bed reactor.[19,66,67] This also reinforces the need for the development of more precise experimental methods to evaluate the catalytic pore size distribution and overall porosity. The PP model predicts that below the macro-porosity threshold of 0.1, the intraparticle flow resistances restrict convective transfer, and intraparticle transport phenomena take place predominantly through diffusion, thus agreeing with literature data.[57−60] In our study, both micro- and macro-porosities were approached as a constant term as non-hierarchical SAPO-34 has a small pore size distribution.[41] Taking the PP model one step further, in each computational cell, the two porosity terms can be expressed using a Gaussian

https://doi.org/10.1021/acsengineeringau.3c00015
ACS Eng. Au 2023, 3, 335−351

size distribution to replicate the impact of particles with pore size ranges. However, this goes beyond the scope of this study. Instead, the full extent of the impact of the intraparticle structure will be examined with the packed beds throughout this study. The macro-porosity of 0.1 is considered moving forward as it demonstrates flow profiles in-between a solid and a completely penetrable particle.

27-Particle Case—Flow Profiles

The radial and axial flow profiles of the main flow parameters, for the 27-particle case, are presented in Figure 4. Contour plots for these profiles are presented in Section 5 of the electronic Supporting Information, along with respective data for the 81-particle case. The comparison of the two models' predictions regarding the reaction rate is based on the EtOH mass fraction at the outlet of the reactor, estimated from the axial length profile. This is because the mass fractions of all products are negligible as the overall EtOH conversion is very small, ≤1.6%.

The PP model predicts velocity magnitude profiles, Figure 4a, that are quantitatively and qualitatively comparable to those of the PR-CFD model. Slight deviations are observed downstream of the last particle row before the outlet, where the PR-CFD predicts higher velocity magnitudes compared to the PP model. Furthermore, as seen in Figures A19 and A21, the wake region, i.e., region of reduced velocity magnitude downstream of the particle(s) is extended in length in the PP model, almost reaching the outlet. This is opposite to what was observed in Yang et al.,[32] where porous particles exhibited a reduced wake length, albeit the macro-porosity used there was ≥0.4. However, as was also observed in their study,[32] some flow pathlines traverse through the intraparticle region, as can be seen Figure A21. The differences between the two approaches at the wake region could further exacerbate at higher Reynolds numbers, where circulations start to appear[76]

The magnitude of velocity in the intraparticle space never drops to zero but instead drops to magnitudes around 1×10^{-4}–1×10^{-3} m/s, or 2–3 orders lower than in the free-flow region. Despite these differences, the PP model reproduces the velocity behavior predicted by the PR-CFD model. This is further highlighted by the PP model being able to reproduce the channeling effect in-between the particles and the reactor wall. Pathlines similar to those of the PR-CFD model are predicted, which converge inward past the last particle row and before the outlet. This emphasizes that, primarily, flow moves through the path of least resistance, avoiding traversing through the intraparticle space.

Fluent does not allow the existence of species within the solid particles, and thus, any flow-specific parameters, such as velocity or pressure, are omitted by default. This limitation is obvious by observing the pressure profile of the PR-CFD case, Figure 4b, which instantly drops to zero within the intraparticle space. On the contrary, as the PP intraparticle region is fluid, static pressure is automatically calculated. In all cases, the PP-predicted static pressure along the axial length presents a "wave-like" profile, which increases prior to meeting the particle(s), decreases through the intraparticle space, and increases again prior to the subsequent particle row. In the free-flow region, i.e., interparticle space, and both along the radial distance and the axial length, the PP-predicted pressure is similar in profiles but larger in magnitude compared to the PR-CFD model predictions. Unlike open-cell foam particles, the pressure drop of the PP is larger than that of the solid particle. We attribute this to the limitation of the Ergun equation to describe permeability of intraparticle structures as it was primarily determined for homogeneous spherical packed beds rather than for individual particles.[73] The limitation of the PR-CFD model to treat the external surface as an impermeable wall completely neglects any morphological parameters that could potentially allow intraparticle viscous flow, driven by local pressure gradients, to exist. Consequently, it might not be suitable to approach the complex morphologies of dual-scale particles. On the contrary, the PP model accounts for both fluid and structural parameters within the intraparticle space, as per Figure A10b of the ESI. Specifically, for the former, fluid velocity, $\vec{v}_{f}$, fluid density, ρ_{f}, and fluid pressure, ∇p, are considered, while for the latter, micro-porosity affects diffusion through the dusty gas model, $D_{DG,\,i}$, and macro-porosity affects the hydrodynamic resistance imposed by the particle through the Ergun equations, eqs 7–9. Therefore, the PP model has the potential to both restrict intraparticle viscous flow, as seen for the intraparticle macro-porosity of 0.001 in Figure 2, and to allow its existence. Moreover, local pore size determines both the micro- and the macro-porosity terms, taking a more realistic approach to replicating complex intraparticle morphologies. In addition, the case studied here uses simplified spherical particles. More complex particle shapes, such as those examined in our CT-scanned bed,[19,22,77] will exhibit different local hydrodynamic behavior, which will affect the reactant accessibility into the pores. Consequently, the ability of the PP model to account for both inter- and intraparticle gradients in the local bed and particle structure, velocity, and pressure can be highly valuable to approach such cases.

The PR-CFD EtOH mass fraction profiles, Figure 4c, are quantitatively similar to those of the PP model, including the near-wall channeling effect which transfers unreactive EtOH towards the outlet. However, in the 27-particle case, the PP-predicted EtOH mass fraction increasingly deviates from the PR-CFD prediction as the flow progresses down the bed, effect which accumulates into a 3% difference between the two models at the outlet. In the 81-particle bed, the PP model suggests that the cumulative deviation of the 27-particle case is restricted only to the first three particle rows and converges past the 3rd row. As a result, at the outlet, the difference in the EtOH mass fraction predicted by the two models only increases to 3.2%. While the PP model can distinguish the physicochemical phenomena associated with the inter- and intraparticle regions, it cannot completely decouple convection and diffusion. As such, similar to the 1-particle case, intraparticle convection plays a role in the predicted reaction rates. To further quantify this, the PP-predicted intraparticle velocity, for the 27-particle case and for the first five rows of the 81-particle case, is presented in Figure 5, with the axial distance referring to the dimensionless particle diameter. Only the particles occupying the exact center of the 3 × 3 orientation are considered for each row.

Velocity presents a parabolic profile within each particle, peaking prior to the particle center, as per Figure 5. The amplitude of this profile increases with increasing particle row, except for the very first row where the flow has yet to establish. Past the third row, in the 81-particle case, the parabolic profile remains constant. These observations are consistent with the PP-predicted EtOH mass fraction behaviors of Figure 4c. In the first 3 particle rows, convection has a beneficial role. Combined with intraparticle diffusion, the small magnitude of intraparticle convection would force more reactants into the

https://doi.org/10.1021/acsengineeringau.3c00015
ACS Eng. Au 2023, 3, 335–351

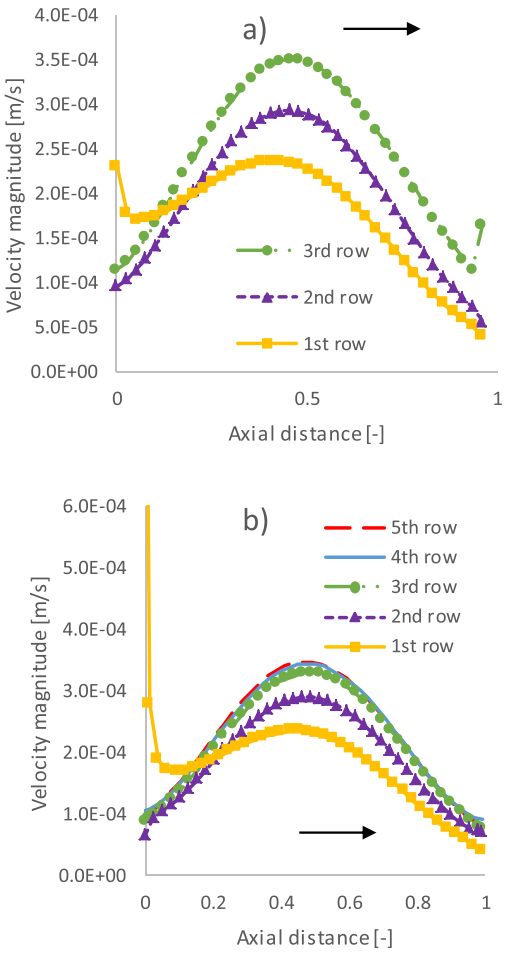

Figure 5. PP-predicted intraparticle velocity magnitude (a) in the 27-particle and (b) in the first five rows of the 81-particle cases. Here, axial distance refers to the particle diameter.

intraparticle space than what would be possible solely through diffusion, but without significantly reducing the residence time. This effect then promotes the reaction rate, especially considering that both R_1 and R_2 are second-order reactions, meaning that a small increase in the local reactant concentration will significantly accelerate the reaction rate. Then in subsequent rows, with the magnitude of intraparticle velocity increasing and establishing, the benefit of increasing the local reactant concentration is counteracted by the reduction of residence time. This competition between increased reactant concentration and reduced resident time results in a roughly constant reaction rate profile. These behaviors demonstrate a complex, two-way interaction between convection and diffusion, with convection having both a beneficial and an inhibitive role.

Intraparticle temperature, Figure 4d, changes due to the involved chemical reactions, with R_1 being exothermic and R_2 being endothermic. The temperature profile predicted by the PR-CFD model follows a "wave-like" pattern. Within the bed structure, temperature peaks in the particle center and reaches a minimum in the interparticle space between two subsequent particles. In the free-flow region, prior to the first particle row and past the last particle row, temperature sharply decreases. The PP-predicted temperature profiles generally follow similar trends to the PR-CFD model predictions. Specifically, temperature peaks within the bed structure, while in the free-flow region, prior to the first particle row and past the last particle row, temperature sharply drops. Here, however, the bed temperature is roughly constant and the "wave-like" pattern observed in the PR-CFD model is almost completely flat. Furthermore, the bed temperature constantly exhibits a higher magnitude. This temperature difference between the two models is primarily focused within the intraparticle space. Because of it, the flow temperature downstream of the PP particle(s) is also higher due to convective heat transfer. Overall, the temperature difference between the two models is negligible in the order of 0.1 K. To understand its origin, the impact of the two primary energy terms, i.e., the heat of reaction and convection, is examined.

27-Particle Case—Reaction and Convection

In this section, the predictions of the two models regarding the contribution of reaction and convection, being the two primary energy terms as per Figure 3, will be compared. Only the 27-particle case is examined because of the resemblance between the 27- and the 81-particle cases.

For reaction, the PP model predicts a lower exothermicity compared to the PR-CFD model, which is further reduced down the bed. The biggest difference is observed in the center of the last particle row and is equal to 4.5%. Thus, exothermicity follows the EtOH mass fraction trend predicted by the two models. With the PP model predicting a faster reaction rate, compared to the PR-CFD model, the rate of the endothermic reaction, R_2, and of ethylene production is also increased, which explains the reduced magnitude of the reaction energy term.

Despite the higher endothermic R_2 rate of the PP model, the PP bed temperature is higher compared to that of the PR-CFD model, as per Figure 4d. This is attributed to convection transferring heat in the intraparticle region. The magnitude of convection, Figure 6b, peaks immediately next to the particle surface. In this region, the flow is relatively stagnant as velocity slows down significantly due to the existence of the particle on the flow path. Consequently, the observed increase is due to the local enthalpy changes from intraparticle reactions. Both PP and PR-CFD models predict very similar convection profiles and trends, with the PP predicting slightly smaller magnitudes. Considering the slight differences observed in velocity and reaction rate profiles, this is reasonable. But the existence of intraparticle convection will result in the transfer of enthalpy within the intraparticle space, as was highlighted by Dixon et al.,[64] which is sufficient to cause the temperature differences observed for the two models.

Parametric Study: WHSV

To further emphasize the impact of intraparticle convection, the 27-particle bed is also investigated at two additional WHSV, equal to 1_{eq} and 3_{eq} h^{-1}. These represent a particle Reynolds number of 9.1 and 11.5, respectively. The radial profiles for velocity, pressure, EtOH mass fraction, and temperature are presented in Figure 7.

Increasing the WHSV results in higher temperatures, pressures, and velocity magnitudes. The PR-CFD predicted that the pressure drop in the free flow region increased by around 3 Pa as WHSV increased from 1_{eq} to 3_{eq}. The PP particle again overpredicted the pressure profile, showcasing a pressure drop increase of 9 Pa. Regarding chemical reactions, in the particle center, i.e., 0 point of X-axis of Figure 7, the PP overpredicted EtOH consumption by 1.5% (1_{eq} h^{-1}), 2% (2_{eq} h^{-1}), and 5.3% (3_{eq} h^{-1}). This showcases that as WHSV

https://doi.org/10.1021/acsengineeringau.3c00015
ACS Eng. Au 2023, 3, 335−351

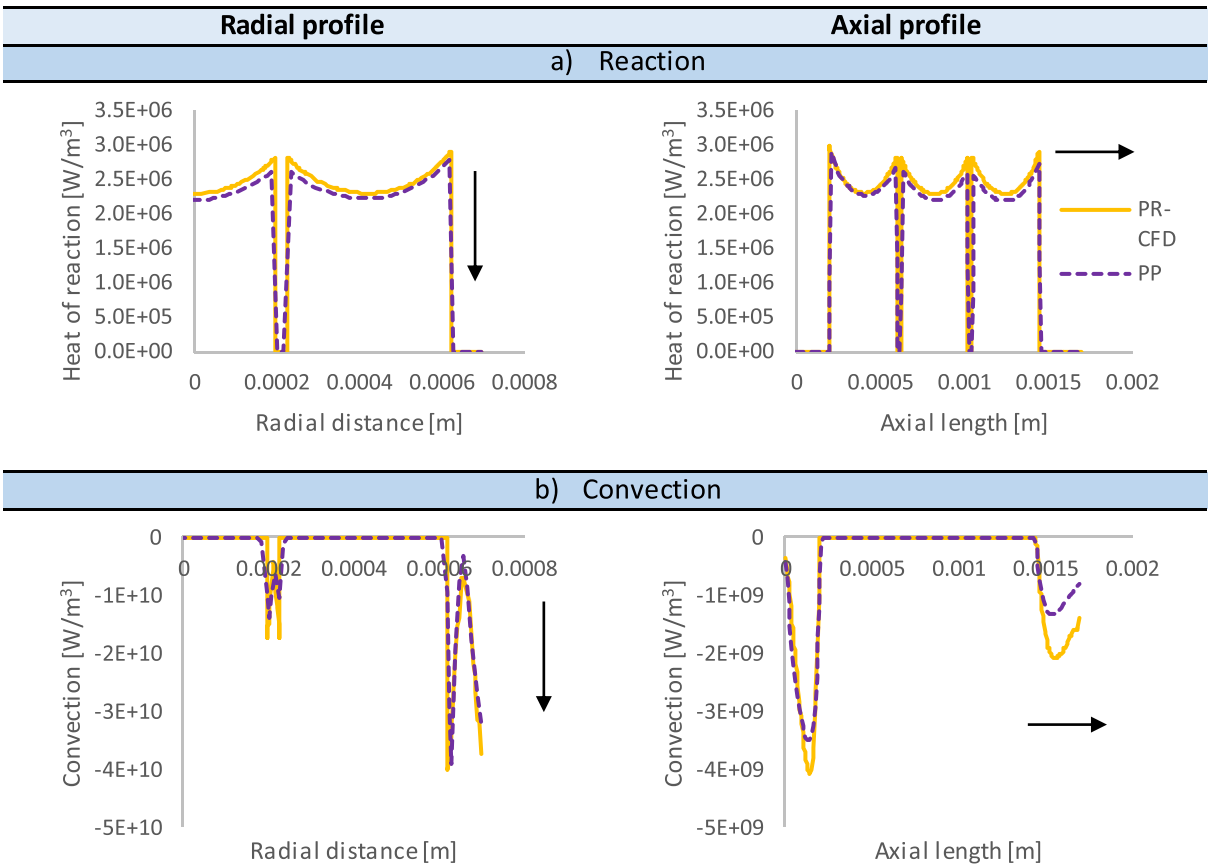

Figure 6. (a) Reaction and (b) convection energy terms for the 27-particle case, as predicted by the PP and the PR-CFD models. All figures share the same legend. The arrows represent the flow direction.

increases, intraparticle convection plays a more prominent role, forcing higher local intraparticle EtOH concentrations which further accelerate the reaction rate. In the same region, temperature differences between the two models increased by 0.03 K (1_{eq} h^{-1}), 0.09 K (2_{eq} h^{-1}), and 0.19 K (3_{eq} h^{-1}). The combined effect of stronger intraparticle convection and faster reactions increased the temperature differences between the two models.

Parametric Study: Exothermicity

In this study, EtOH dehydration was chosen as the test case, replicating our experimental conditions, reaction which follows an exothermic DEE formation step and an endothermic ethylene formation step. At the conditions studied, DEE formation is the predominant step, whose exothermicity is mild, having an enthalpy change of −24 kJ/mol. In addition, there is a considerable fraction of inert N_2 gas driving the flow, 77% in terms of mass fractions, at a temperature equal to that of the bed and of the reactants. Given its inert nature and its extensive presence, it quenches the produced exothermic heat, driving it away from the particle(s). As a result, the temperature variations observed throughout this study were miniscule, below 1 K. Studying the PP at a scenario of intense exothermicity will yield key observations regarding the extent of the convection's impact. With that in mind, the DEE enthalpy of formation was fictionally increased by an order of magnitude, i.e., −2530 instead of −253 kJ/mol, which boosted the exothermicity of R_1 to −2.3 MJ/mol. Unfortunately, this resulted in an unstable simulation which never converged, even after 8k iterations. While convergence could be aided through the under-relaxation factors, it was decided to keep the same solution setup as the rest of the paper. The resulting profiles for the 27-particle case are presented in Figure 8.

The excessive exothermicity exaggerated the differences between the two particle models. Specifically, the intense heat released from the enhanced exothermicity led to runaway conditions, effect most prominent in the temperature and EtOH mass fraction profiles. In the particle center, i.e., 0 point of *X*-axis, the PP reaches a temperature difference with the solid particle equal to 127 K, corresponding to an increase of 25%. In the same region, the PP-predicted EtOH consumption is increased by 33%, compared to the solid particle. The enhanced intraparticle reaction rate thus changed the local species concentrations, causing increased flow pressures.

These results highlight that intraparticle convection cannot be neglected at strongly exothermic reactions as it can have a detrimental effect on the resulting fixed bed behavior. This demonstrates that the potential existence of even a small amount of intraparticle convection can significantly change all aspects of flow dynamics and chemistry. It also reinforces the importance and the need for the development of a systematic experimental methodology to accurately measure the pore size distribution and porosity of individual catalytic particles. Identifying the connection between the pore structure and intraparticle convection will be vital for future reactor engineering. The quantification of the pore size of the intraparticle networks formed within porous particles will allow CFD simulations to more accurately estimate the role of intraparticle convection. Furthermore, this report focused on quantifying intraparticle convection in a small packed-bed

https://doi.org/10.1021/acsengineeringau.3c00015
ACS Eng. Au 2023, 3, 335−351

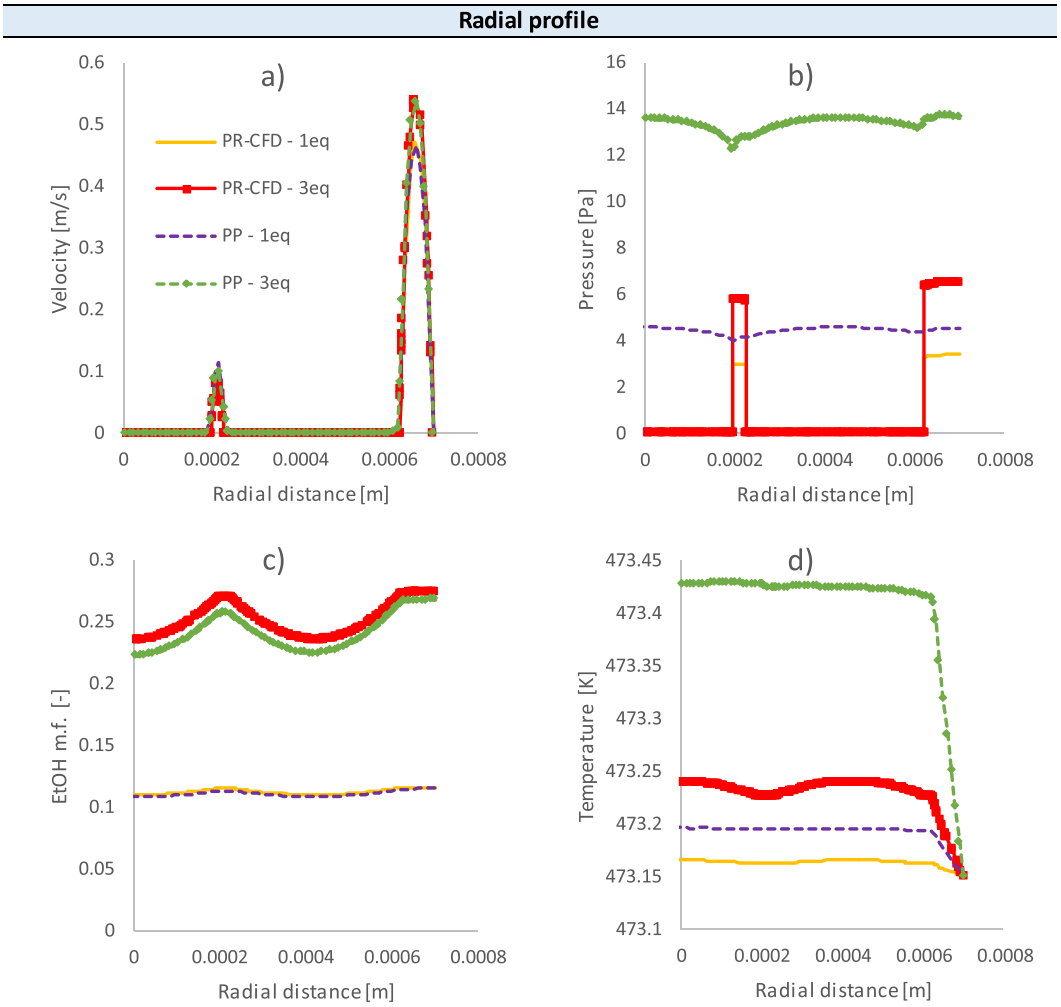

Figure 7. Radial profiles of (a) velocity, (b) pressure, (c) EtOH mass fraction, and (d) temperature for the PR-CFD and PP models as a result of different WHSV flow rates.

setup. CFD validation with the full bed experimental setup will be investigated in our future work.

Scalability

Aside from the physicochemical phenomena, the two meshing approaches of the PR-CFD and PP models allow the comparison of the computational resources between particle-resolved tetrahedral elements and hexahedral Cartesian grids. With the imperative need to transition computational models to simulate industrial-scale reactors, thus accelerating our emission reduction goals, it is key to identify the most prominent meshing and modeling approaches for scaling-up CFD models. The computational demands of the three particle cases are judged based on four metrics, the file size, the iteration number required for convergence, the computational time, and the total RAM usage. File size affects how easy handling and storing the produced data is, iteration number affects the stability of the solution process and the iterations needed for full convergence, and the computational time indicates the physical time duration needed for full convergence. The RAM usage indicates the hardware requirements for the simulated process. The computational time required for the two models to simulate the three geometries considered is presented in Figure 9, and all computational resources can be seen in Table 1. The parenthesis next to the PP results is the percentage comparison with the respective PR-CFD metric. All simulations of the three baseline cases took place on the IRIDIS 5 high-performance computing facility, utilizing 1 Intel Xeon 6130 2.1 GHz CPU with 139 GB of RAM.

The significant reduction in the resource requirements of the PP model, when compared to those of the PR-CFD model, is evident in Table 1. The PP model is significantly easier to handle (smaller file size), more stable (less iterations), and faster (less computational time), compared to the PR-CFD model. Furthermore, the hardware requirements are significantly lower as well. Compared to the PR-CFD, the biggest reduction in the computational time achieved by the PP model is equal to 75% for the 81-particle case. Critically, the PR-CFD computational time requirements exponentially increase with increasing number of particles, whereas a linear increase is observed for the PP model.

The limitation of PR-CFD models is their extensive computational resource requirements[7,8,78] as each individual particle must be resolved. To mesh the complex topological structured produced by PR-CFD models, unstructured tetrahedral or polyhedral cells are necessary to accurately discretize the computational domain.[79] Instead, models that do not explicitly resolve catalytic particles, such as the PP model of this study and the model of Das et al.,[53] can utilize much simpler meshing approaches, ideally utilizing hexahedral cells.

https://doi.org/10.1021/acsengineeringau.3c00015
ACS Eng. Au 2023, 3, 335−351

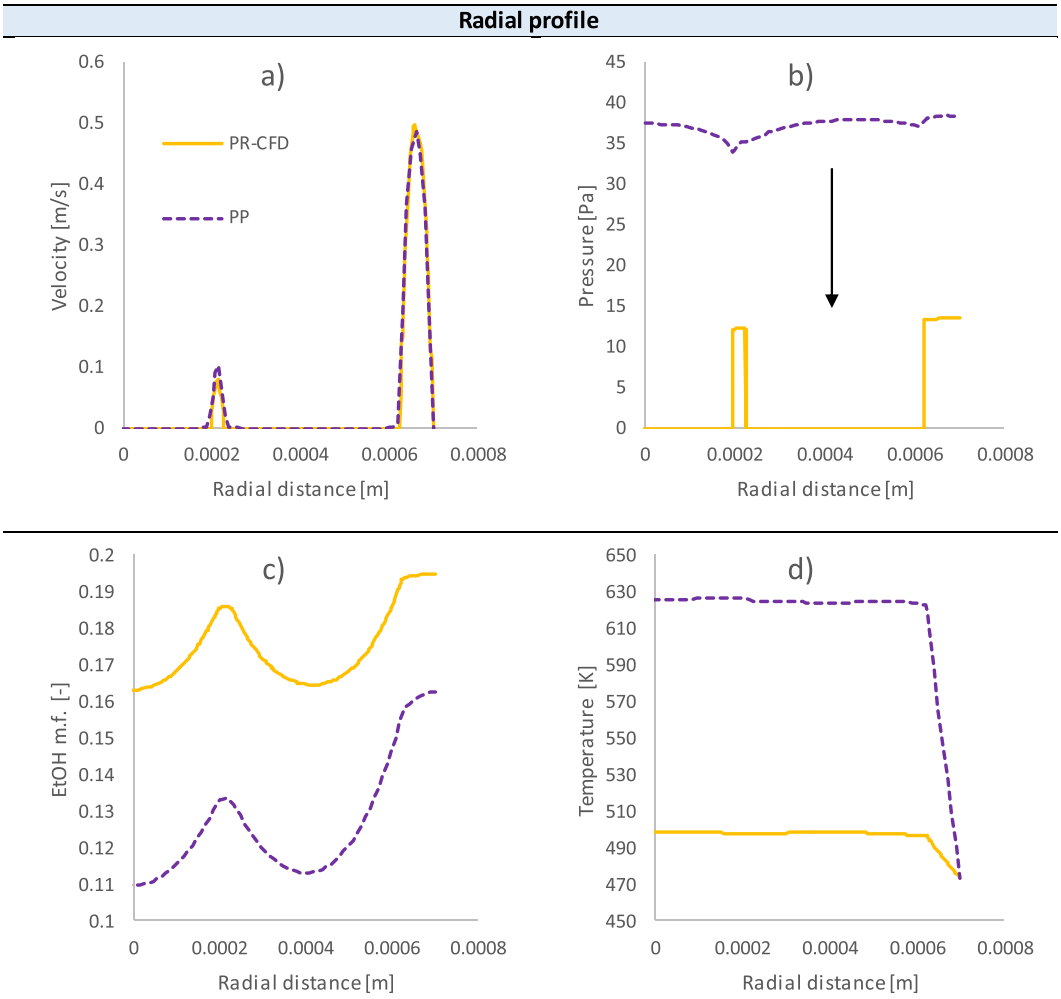

Figure 8. Radial profiles of (a) velocity, (b) pressure, (c) EtOH mass fraction, and (d) temperature for the PR-CFD and PP models as a result of increased exothermicity.

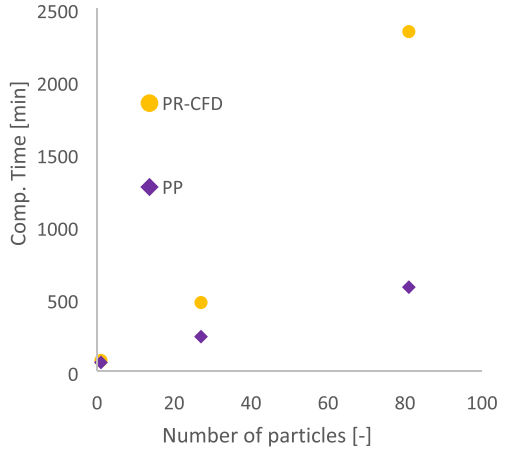

Figure 9. Computational time requirements for the PR-CFD and the PP models for all three particle geometries.

Table 1. Computational Resource Requirements of the PR-CFD and PP Models for the 1-, 27-, and 81-Particle Cases[a]

	file size [Gb]	iterations [−]	computational time [min]	RAM utilization [Gb]
		1-Particle Case		
PR-CFD	1.1	2162	73	6.9
PP	0.9 (−18%)	1981 (−8%)	59 (−19%)	5.3 (−23%)
		27-Particle Case		
PR-CFD	10.05	2014	472	36.9
PP	4.4 (−56%)	1609 (−20%)	237 (−50%)	19.7 (−47%)
		81-Particle Case		
PR-CFD	28.1	1919	2340	79
PP	11.03 (−61%)	1583 (−18%)	578 (−75%)	40.3 (−49%)

[a]These simulations were performed with 1 Intel Xeon 6130 2.1 GHz CPU with 139 GB of RAM.

The results presented here reinforce the more efficient computational resource utilization achieved by hexahedral cells when those are compared to tetrahedral cells.[12,80] It would be interesting as a next step to compare the computational demands of the PP model with a PR-CFD mesh which utilizes the polyhedral approach of Sosnowski et al.[81] Regardless, the reduction the PP model achieved in its computational demands could potentially allow it to simulate industrial-scale reactors with included intraparticle phenomena, or applications with more complex geometries, e.g., asymmetric and poly-dispersed beds, where mesh is a considerable constraint. However, more study is necessary

https://doi.org/10.1021/acsengineeringau.3c00015
ACS Eng. Au 2023, 3, 335−351

prior to the PP model being utilized in such applications that goes beyond this paper. Specifically, with industrial reactors being predominantly operated at turbulent conditions, the behavior of the PP model in such flow regimes should be clearly understood. This is especially critical to be combined with a mesh-independency study, similar to the one presented in Section 4.1 of the electronic Supporting Information, as the boundary layer for a turbulent case would be more complex to be captured than that of a laminar case. Regardless, the developed PP model investigated here is highly valuable for meso/-macro-pore particles where intraparticle convection could play a key role. However, similar models where the particle are not resolved, thus utilizing a hexahedral grid, yet a no-slip flow boundary condition was applied on their surface, restricting intraparticle convection, have been developed in the literature.[76,82−85] The study of Das et al. is a great example of this.[53] Consequently, depending on the CFD model requirements and the experimental application they are applied to, non-resolved models with Cartesian grids offer a wide flexibility, enabling both the study of impermeable solid particles and of multi-pore-scale particles, with significantly reduced computational resources.

CONCLUSIONS

The recent development of catalytic particles with multi-scale porosities drives the need for more advanced CFD models that are capable of reproducing such intraparticle morphologies. Such multi-scale catalytic particles consist of macro-pores that enhance the intraparticle heat and mass transfer and micro-pores that considerably increase the exposed active surface area, thus boosting the reactivity. Catalytic particles with low intraparticle macro-porosities, ≤0.5, have been traditionally approached in CFD studies purely as solid. As a result, intraparticle convection was completely neglected. Its potential existence in such dual-scale porous systems could give rise to some unique phenomena that cannot be reproduced if the particle is approached as purely solid. This necessitates CFD models that can reproduce the intraparticle multi-pore-scale structure without strictly restricting intraparticle convection. Here, such a model is developed by approaching particles as porous with two distinct porosity terms, specifically a macro-porosity responsible for the hydrodynamic profile of the particles and a micro-porosity responsible for diffusion and reaction. By comparing the flow profiles within beds formed by porous and by solid particles, the impact of intraparticle convection can be determined.

Through this comparison, it was identified that intraparticle convection can play a pivotal role, showcasing a complex interaction with intraparticle heat and mass transfer, as well as with diffusion and reaction. Specifically, convection increased the transfer of enthalpy within the intraparticle space, increasing the local temperature. Furthermore, it accelerated the transfer of species within the particles, compared to what would be possible solely through diffusion, thus enhancing the reaction rate. Through a parametric study, it was identified that, at highly exothermic reactions, these phenomena are further exaggerated. Consequently, experimentally identifying and characterizing the intraparticle network and pore size distribution within catalytic particles is key for the advancement of more accurate computational fluid dynamics models. Furthermore, the development of flexible CFD models that could either restrict or enable intraparticle convection, depending on the application, is critical to allow CFD models to reproduce the modern multi-pore-scale catalysts.

ASSOCIATED CONTENT

Supporting Information

The Supporting Information is available free of charge at https://pubs.acs.org/doi/10.1021/acsengineeringau.3c00015.

Experimental configuration and computational model setup (PDF)

AUTHOR INFORMATION

Corresponding Author

Lindsay-Marie Armstrong − *School of Engineering, University of Southampton, Southampton SO17 1BJ, U.K.*; Email: L.Armstrong@soton.ac.uk

Authors

Stylianos Kyrimis − *School of Engineering and School of Chemistry, University of Southampton, Southampton SO17 1BJ, U.K.*; orcid.org/0000-0002-6195-9421

Matthew E. Potter − *School of Chemistry, University of Southampton, Southampton SO17 1BJ, U.K.*; orcid.org/0000-0001-9849-3306

Robert Raja − *School of Chemistry, University of Southampton, Southampton SO17 1BJ, U.K.*; orcid.org/0000-0002-4161-7053

Complete contact information is available at: https://pubs.acs.org/10.1021/acsengineeringau.3c00015

Notes

The authors declare no competing financial interest.

ACKNOWLEDGMENTS

The authors would like to thank the Southampton Marine & Maritime Institute for their funding. In addition, the authors would like to acknowledge the use of the IRIDIS 5 High Performance Computing Facility and associated support services at the University of Southampton in the completion of this work. Finally, they would like to acknowledge the contribution of Evangeline McShane and of Maciej Walerowski for running the N_2 physisorption results.

NOMENCLATURE

A_j	pre-exponential factor of reaction "j" [m^3/kmol·s]
C_{Inert}	inertial resistance in porous medium [m^{-1}]
$D_{eff,\,i}$	diffusion coefficient of species "i" [m^2/s]
ΔH	enthalpy change [J/kmol]
d_p	particle diameter [m]
d_{pore}	intraparticle pore diameter [m]
E_j	activation energy of reaction "j" [J/kmol]
h	enthalpy [J/kmol]
$\vec{J}_i$	diffusion flux [kg/m^2·s]
k_f	thermal conductivity of a fluid [W/m·K]
k_s	thermal conductivity of a solid [W/m·K]
$M_{w,\,i}$	molar weight of species "i" [kg/kmol]
R	universal gas constant [J/kmol·K]
$R_{i,\,j}$	reaction rate of species "i" in reaction "j" [kg/m^3·s]
S_h	energy source [W/m^3]
$\vec{S}_i$	momentum source [Pa]
T_f	fluid temperature [K]

https://doi.org/10.1021/acsengineeringau.3c00015
ACS Eng. Au 2023, 3, 335−351

T_s	solid temperature [K]
$\vec{v}$	velocity vector [m/s]
v_{PM}	superficial velocity within the porous particle [m/s]
V_{Bed}	volume of catalytic bed [m^3]
V_{pores}	volume of intraparticle pores [m^3]
$V_{macro\ -\ pores}$	volume of intraparticle macro-pores [m^3]
$V_{meso\ -\ pores}$	volume of intraparticle meso-pores [m^3]
$V_{micro\ -\ pores}$	volume of intraparticle micro-pores [m^3]
V_{Solid}	volume of a solid material [m^3]

Greek Symbols

α	viscous resistance in porous medium [m^2]
ε_{Inter}	interparticle porosity/bed void fraction [−]
ε_{Intra}	intraparticle porosity [−]
ε_{macro}	intraparticle macro-porosity [−]
ε_{meso}	intraparticle meso-porosity [−]
ε_{micro}	intraparticle micro-porosity [−]
$\eta_{i,j}$	stoichiometric coefficient of species "i" in reaction "j" [−]
μ_f	fluid viscosity [kg/m·s]
ρ_f	fluid density [kg/m^3]
ρ_s	solid density [kg/m^3]
$\bar{\bar{\tau}}_f$	stress tensor [Pa]
τ_{Intra}	intraparticle tortuosity [−]
φ_i	scalar quantity "i" (mass fraction of species "i") [−]

REFERENCES

(1) Zhang, M.; Yu, Y. Dehydration of Ethanol to Ethylene. *Ind. Eng. Chem. Res.* **2013**, *52*, 9505−9514.

(2) Bozzano, G.; Manenti, F. Efficient methanol synthesis: Perspectives, technologies and optimization strategies. *Prog. Energy Combust. Sci.* **2016**, *56*, 71−105.

(3) Missen, R. W., Mims, C. A.; Saville, B. A. *Introduction to Chemical Reaction Engineering and Kinetics*; Wiley, 1999.

(4) Atmakidis, T.; Kenig, E. Y. CFD-based analysis of the wall effect on the pressure drop in packed beds with moderate tube/particle diameter ratios in the laminar flow regime. *Chem. Eng. J.* **2009**, *155*, 404−410.

(5) Plutschack, M. B.; Pieber, B.; Gilmore, K.; Seeberger, P. H. The Hitchhiker's Guide to Flow Chemistry. *Chem. Rev.* **2017**, *117*, 11796−11893.

(6) Noorman, S.; Gallucci, F.; van Sint Annaland, M.; Kuipers, J. A. M. A theoretical investigation of CLC in packed beds. Part 1: Particle model. *Chem. Eng. J.* **2011**, *167*, 297−307.

(7) Dixon, A. G.; Nijemeisland, M.; Stitt, E. H. Packed Tubular Reactor Modeling and Catalyst Design using Computational Fluid Dynamics. *Comput. Fluid Dyn.* **2006**, *31*, 307−389.

(8) Wehinger, G. D.; Eppinger, T.; Kraume, M. Detailed numerical simulations of catalytic fixed-bed reactors: Heterogeneous dry reforming of methane. *Chem. Eng. Sci.* **2015**, *122*, 197−209.

(9) Dixon, A. G.; Partopour, B. Computational Fluid Dynamics for Fixed Bed Reactor Design. *Annu. Rev. Chem. Biomol. Eng.* **2020**, *11*, 109−130.

(10) Partopour, B.; Dixon, A. G. 110th Anniversary: Commentary: CFD as a Modeling Tool for Fixed Bed Reactors. *Ind. Eng. Chem. Res.* **2019**, *58*, 5733−5736.

(11) Dixon, A. G.; Nijemeisland, M. CFD as a Design Tool for Fixed-Bed Reactors. *Ind. Eng. Chem. Res.* **2001**, *40*, 5246−5254.

(12) Jurtz, N.; Kraume, M.; Wehinger, G. D. Advances in fixed-bed reactor modeling using particle-resolved computational fluid dynamics (CFD). *Rev. Chem. Eng.* **2019**, *35*, 139−190.

(13) Kyrimis, S.; Potter, M. E.; Raja, R.; Armstrong, L.-M. Understanding catalytic CO2 and CO conversion into methanol using computational fluid dynamics. *Faraday Discuss.* **2021**, *230*, 100−123.

(14) Mueller, G. E. Numerically packing spheres in cylinders. *Powder Technol.* **2005**, *159*, 105−110.

(15) Theuerkauf, J.; Witt, P.; Schwesig, D. Analysis of particle porosity distribution in fixed beds using the discrete element method. *Powder Technol.* **2006**, *165*, 92−99.

(16) von Seckendorff, J.; Hinrichsen, O. Review on the structure of random packed-beds. *Can. J. Chem. Eng.* **2021**, *99*, S703−S733.

(17) Dixon, A. G. Local transport and reaction rates in a fixed bed reactor tube: Exothermic partial oxidation of ethylene. *Chem. Eng. Sci.* **2021**, *231*, No. 116305.

(18) Dixon, A. G. Local transport and reaction rates in a fixed bed reactor tube: Endothermic steam methane reforming. *Chem. Eng. Sci.* **2017**, *168*, 156−177.

(19) Kyrimis, S.; Rankin, K. E.; Potter, M. E.; Raja, R.; Armstrong, L.-M. Towards realistic characterisation of chemical reactors: An in-depth analysis of catalytic particle beds produced by sieving. *Adv. Powder Technol.* **2023**, *34*, No. 103932.

(20) Zhang, M.; Dong, H.; Geng, Z. Computational study of particle packing process and fluid flow inside Polydisperse cylindrical particles fixed beds. *Powder Technol.* **2019**, *354*, 19−29.

(21) Boccardo, G.; Augier, F.; Haroun, Y.; Ferré, D.; Marchisio, D. L. Validation of a novel open-source work-flow for the simulation of packed-bed reactors. *Chem. Eng. J.* **2015**, *279*, 809−820.

(22) Kyrimis, S.; Raja, R.; Armstrong, L.-M. Hydrodynamic profiles of computed tomography-scanned polydispersed beds produced by sieving. *Proceedings of the 10th International Conference on Fluid Flow, Heat and Mass Transfer (FFHMT '23)*, 2023.

(23) Partopour, B.; Dixon, A. G. Integrated multiscale modeling of fixed bed reactors: Studying the reactor under dynamic reaction conditions. *Chem. Eng. J.* **2019**, *377*, 119738.

(24) Wehinger, G. D.; Fütterer, C.; Kraume, M. Contact Modifications for CFD Simulations of Fixed-Bed Reactors: Cylindrical Particles. *Ind. Eng. Chem. Res.* **2017**, *56*, 87−99.

(25) Partopour, B.; Dixon, A. G. An integrated workflow for resolved-particle packed bed models with complex particle shapes. *Powder Technol.* **2017**, *322*, 258−272.

(26) Rodrigues, S. J.; Vorhauer-Huget, N.; Richter, T.; Tsotsas, E. Influence of Particle Shape on Tortuosity of Non-Spherical Particle Packed Beds. *Processes* **2023**, *11*, 3. Available: https://www.mdpi.com/2227-9717/11/1/3

(27) Uebel, K.; Rößger, P.; Prüfert, U.; Richter, A.; Meyer, B. CFD-based multi-objective optimization of a quench reactor design. *Fuel Process. Technol.* **2016**, *149*, 290−304.

(28) Kyrimis, S.; Le Clercq, P.; Brendelberger, S. 3D modelling of a solar thermochemical reactor for MW scaling-up studies. *AIP Conf. Proc.* **2019**, *2126*, 180013.

(29) Van Cauwenberge, D. J.; Schietekat, C. M.; Floré, J.; Van Geem, K. M.; Marin, G. B. CFD-based design of 3D pyrolysis reactors: RANS vs. LES. *Chem. Eng. J.* **2015**, *282*, 66−76.

(30) Zhou, X.; Duan, Y.; Huai, X.; Li, X. 3D CFD modeling of acetone hydrogenation in fixed bed reactor with spherical particles. *Particuology* **2013**, *11*, 715−722.

(31) Solsvik, J.; Jakobsen, H. A. A numerical study of a two property catalyst/sorbent pellet design for the sorption-enhanced steam−methane reforming process: Modeling complexity and parameter sensitivity study. *Chem. Eng. J.* **2011**, *178*, 407−422.

(32) Yang, X.; Wang, S.; Jin, H.; He, Y. Pore-scale simulation of flow and mass transfer characteristics of porous particle. *Chem. Eng. Sci.* **2023**, *267*, No. 118301.

(33) Dong, Y.; Keil, F. J.; Korup, O.; Rosowski, F.; Horn, R. Effect of the catalyst pore structure on fixed-bed reactor performance of partial oxidation of n-butane: A simulation study. *Chem. Eng. Sci.* **2016**, *142*, 299−309.

(34) Ackermann, S.; Takacs, M.; Scheffe, J.; Steinfeld, A. Reticulated porous ceria undergoing thermochemical reduction with high-flux irradiation. *Int. J. Heat Mass Transfer* **2017**, *107*, 439−449.

(35) Wang, Y.; Arandiyan, H.; Scott, J.; Bagheri, A.; Dai, H.; Amal, R. Recent advances in ordered meso/macroporous metal oxides for

https://doi.org/10.1021/acsengineeringau.3c00015
ACS Eng. Au 2023, 3, 335−351

heterogeneous catalysis: a review. *J. Mater. Chem. A* **2017**, *5*, 8825−8846.
(36) Fogler, S. H. *Elements of Chemical Reaction Engineering*, 5th ed.; Pearson, 2016.
(37) Nauman, E. B. *Chemical Reactor Design, Optimization, and Scaleup*, 2nd ed.; Wiley, 2008.
(38) Ariga, K.; Vinu, A.; Yamauchi, Y.; Ji, Q.; Hill, J. P. Nanoarchitectonics for Mesoporous Materials. *Bull. Chem. Soc. Jpn.* **2012**, *85*, 1−32.
(39) Sun, Q.; Dai, Z.; Meng, X.; Xiao, F.-S. Porous polymer catalysts with hierarchical structures. *Chem. Soc. Rev.* **2015**, *44*, 6018−6034.
(40) Parlett, C. M. A.; Wilson, K.; Lee, A. F. Hierarchical porous materials: catalytic applications. *Chem. Soc. Rev.* **2013**, *42*, 3876−3893.
(41) Sun, Q.; Wang, N.; Guo, G.; Chen, X.; Yu, J. Synthesis of tri-level hierarchical SAPO-34 zeolite with intracrystalline micro−meso−macroporosity showing superior MTO performance. *J. Mater. Chem. A* **2015**, *3*, 19783−19789.
(42) Chen, L.-H.; Sun, M.-H.; Wang, Z.; Yang, W.; Xie, Z.; Su, B.-L. Hierarchically Structured Zeolites: From Design to Application. *Chem. Rev.* **2020**, *120*, 11194−11294.
(43) Koohsaryan, E.; Anbia, M. Nanosized and hierarchical zeolites: A short review. *Chin. J. Catal.* **2016**, *37*, 447−467.
(44) Kee, R. J.; Coltrin, M. E.; Peter, G.; Zhu, H. *Chemically Reacting Flow: Theory, Modeling, and Simulation*, 2nd ed.; Wiley, 2017.
(45) Bardestani, R.; Patience, G. S.; Kaliaguine, S. Experimental methods in chemical engineering: specific surface area and pore size distribution measurements—BET, BJH, and DFT. *Can. J. Chem. Eng.* **2019**, *97*, 2781−2791.
(46) Simaioforidou, A.; Kostas, V.; Karakassides, M. A.; Louloudi, M. Surface chemical modification of macroporous and mesoporous carbon materials: Effect on their textural and catalytic properties. *Microporous Mesoporous Mater.* **2019**, *279*, 334−344.
(47) Tan, L.; Tan, B. Functionalized hierarchical porous polymeric monoliths as versatile platforms to support uniform and ultrafine metal nanoparticles for heterogeneous catalysis. *Chem. Eng. J.* **2020**, *390*, No. 124485.
(48) Das, S.; Sneijders, S.; Deen, N. G.; Kuipers, J. A. M. Drag and heat transfer closures for realistic numerically generated random open-cell solid foams using an immersed boundary method. *Chem. Eng. Sci.* **2018**, *183*, 260−274.
(49) Chandra, V.; Das, S.; Peters, E. A. J. F.; Kuipers, J. A. M. Direct numerical simulation of hydrodynamic dispersion in open-cell solid foams. *Chem. Eng. J.* **2019**, *358*, 1305−1323.
(50) Das, S.; Deen, N. G.; Kuipers, J. A. M. Direct numerical simulation for flow and heat transfer through random open-cell solid foams: Development of an IBM based CFD model. *Catal. Today* **2016**, *273*, 140−150.
(51) Das, S.; Panda, A.; Deen, N. G.; Kuipers, J. A. M. A sharp-interface Immersed Boundary Method to simulate convective and conjugate heat transfer through highly complex periodic porous structures. *Chem. Eng. Sci.* **2018**, *191*, 1−18.
(52) George, G. R.; et al. Influence of Foam Morphology on Flow and Heat Transport in a Random Packed Bed with Metallic Foam Pellets—An Investigation Using CFD. *Materials* **2022**, *15*, 3754.
(53) Das, S.; Deen, N. G.; Kuipers, J. A. M. Multiscale modeling of fixed-bed reactors with porous (open-cell foam) non-spherical particles: Hydrodynamics. *Chem. Eng. J.* **2018**, *334*, 741−759.
(54) Wehinger, G. D.; Kolaczkowski, S. T.; Schmalhorst, L.; Beton, D.; Torkuhl, L. Modeling fixed-bed reactors from metal-foam pellets with detailed CFD. *Chem. Eng. J.* **2019**, *373*, 709−719.
(55) George, G. R.; et al. Radial heat transport in a fixed-bed reactor made of metallic foam pellets: Experiment and particle-resolved computational fluid dynamics. *Int. J. Heat Mass Transfer* **2022**, *197*, No. 123376.
(56) Solsvik, J.; Jakobsen, H. A. Impacts on the Reactor Performance of Intra-Particle Multicomponent Mass Diffusion Limitations: Knudsen Diffusion. *Energy Procedia* **2012**, *26*, 116−124.
(57) Donaubauer, P. J.; Hinrichsen, O. A Monte-Carlo-based sensitivity analysis of multicomponent diffusion in porous catalysts. *Chem. Eng. Sci.* **2018**, *185*, 282−291.
(58) A., Richter, P. A., Nikrityuk, B., Meyer, *Three-dimensional calculation of a chemically reacting porous particle moving in a hot O2/CO2 atmosphere*, *83*, 244−258, 2015, DOI: 10.1016/j.ijheatmasstransfer.2014.11.090.
(59) Rout, K. R.; Solsvik, J.; Nayak, A. K.; Jakobsen, H. A. A numerical study of multicomponent mass diffusion and convection in porous pellets for the sorption-enhanced steam methane reforming and desorption processes. *Chem. Eng. Sci.* **2011**, *66*, 4111−4126.
(60) Solsvik, J.; Jakobsen, H. A. A Survey of Multicomponent Mass Diffusion Flux Closures for Porous Pellets: Mass and Molar Forms. *Transp. Porous Media* **2012**, *93*, 99−126.
(61) Donaubauer, P. J.; Hinrichsen, O. Evaluation of Effectiveness Factors for Multicomponent Diffusion Models Inside 3D Catalyst Shapes. *Ind. Eng. Chem. Res.* **2019**, *58*, 110−119.
(62) Chen, X.-M.; Xiao, J.; Zhu, Y.-P.; Luo, Z.-H. Intraparticle Mass and Heat Transfer Modeling of Methanol to Olefins Process on SAPO-34: A Single Particle Model. *Ind. Eng. Chem. Res.* **2013**, *52*, 3693−3707.
(63) Spallina, V.; Marinello, B.; Gallucci, F.; Romano, M. C.; Van Sint Annaland, M. Chemical looping reforming in packed-bed reactors: Modelling, experimental validation and large-scale reactor design. *Fuel Process. Technol.* **2017**, *156*, 156−170.
(64) Dixon, A. G.; Taskin, M. E.; Nijemeisland, M.; Stitt, E. H. CFD Method To Couple Three-Dimensional Transport and Reaction inside Catalyst Particles to the Fixed Bed Flow Field. *Ind. Eng. Chem. Res.* **2010**, *49*, 9012−9025.
(65) Dixon, A. G.; Ertan Taskin, M.; Hugh Stitt, E.; Nijemeisland, M. 3D CFD simulations of steam reforming with resolved intraparticle reaction and gradients. *Chem. Eng. Sci.* **2007**, *62*, 4963−4966.
(66) Potter, M. E.; Armstrong, L.-M.; Raja, R. Combining catalysis and computational fluid dynamics towards improved process design for ethanol dehydration. *Catal. Sci. Technol.* **2018**, *8*, 6163−6172.
(67) Potter, M. E.; Armstrong, L.-M.; Carravetta, M.; Mezza, T. M.; Raja, R. Designing Multi-Dopant Species in Microporous Architectures to Probe Reaction Pathways in Solid-Acid Catalysis. *Front. Chem.* **2020**, *8*, 171.
(68) ANSYS Inc.. ANSYS Fluent Theory Guide. *Fluent Theory Guide*, Release 15.0, November 2013, 2013.
(69) Gao, M.; et al. A modeling study on reaction and diffusion in MTO process over SAPO-34 zeolites. *Chem. Eng. J.* **2019**, *377*, 119668.
(70) Kolaczkowski, S. T.; Chao, R.; Awdry, S.; Smith, A. Application of a CFD Code (FLUENT) to Formulate Models of Catalytic Gas Phase Reactions in Porous Catalyst Pellets. *Chem. Eng. Res. Des.* **2007**, *85*, 1539−1552.
(71) Hite, R. H.; Jackson, R. Pressure gradients in porous catalyst pellets in the intermediate diffusion regime. *Chem. Eng. Sci.* **1977**, *32*, 703−709.
(72) ANSYS Inc. ANSYS Fluent User's Guide. *Fluent User's Guide*, Release 15.0, November 2013, 2013.
(73) Ergun, S. Fluid flow through packed columns. *Chem. Eng. Prog.* **1952**, *48*, 89−94. Available: https://ci.nii.ac.jp/naid/10003393451/en/
(74) K. S. W., Sing; et al. Characterization of Solid Catalysts: Sections 3.1.1−3.1.3. In *Handbook of Heterogeneous Catalysis*; Ertl, G., Knözinger, H.; Weitkamp, J., eds., 2008.
(75) Peng, Z.; Doroodchi, E.; Moghtaderi, B. Heat transfer modelling in Discrete Element Method (DEM)-based simulations of thermal processes: Theory and model development. *Prog. Energy Combust. Sci.* **2020**, *79*, No. 100847.
(76) Lu, J.; Das, S.; Peters, E. A. J. F.; Kuipers, J. A. M. Direct numerical simulation of fluid flow and mass transfer in dense fluid-particle systems with surface reactions. *Chem. Eng. Sci.* **2018**, *176*, 1−18.

(77) Kyrimis, S.; Raja, R.; Armstrong, L.-M. Image processing of computed tomography scanned poly-dispersed beds for computational fluid dynamic studies. *Adv. Powder Technol.* **2023**, in press, DOI: 10.1016/j.apt.2023.104199.
(78) Jajcevic, D.; Siegmann, E.; Radeke, C.; Khinast, J. G. Large-scale CFD−DEM simulations of fluidized granular systems. *Chem. Eng. Sci.* **2013**, *98*, 298−310.
(79) Zhang, Y.; Ding, Y.; Christofides, P. D. Multiscale computational fluid dynamics modeling of thermal atomic layer deposition with application to chamber design. *Chem. Eng. Res. Des.* **2019**, *147*, 529−544.
(80) Biswas, R.; Strawn, R. C. Tetrahedral and hexahedral mesh adaptation for CFD problems. *Appl. Numer. Math.* **1998**, *26*, 135−151.
(81) Sosnowski, M.; Krzywanski, J.; Grabowska, K.; Gnatowska, R. Polyhedral meshing in numerical analysis of conjugate heat transfer. *EPJ Web Conf.* **2018**, *180*, No. 02096.
(82) Verzicco, R. Immersed Boundary Methods: Historical Perspective and Future Outlook. *Annu. Rev. Fluid Mech.* **2023**, *55*, 129−155.
(83) Xiao, W.; Zhang, H.; Luo, K.; Mao, C.; Fan, J. Immersed boundary method for multiphase transport phenomena. *Rev. Chem. Eng.* **2022**, *38*, 363−405.
(84) Sulaiman, M.; Hammouti, A.; Climent, E.; Wachs, A. Coupling the fictitious domain and sharp interface methods for the simulation of convective mass transfer around reactive particles: Towards a reactive Sherwood number correlation for dilute systems. *Chem. Eng. Sci.* **2019**, *198*, 334−351.
(85) Maitri, R. V.; Das, S.; Kuipers, J. A. M.; Padding, J. T.; Peters, E. A. J. F. An improved ghost-cell sharp interface immersed boundary method with direct forcing for particle laden flows. *Comput. Fluids* **2018**, *175*, 111−128.